Environmental Science Nano

PAPER

View Article Online
View Journal | View Issue



Cite this: *Environ. Sci.: Nano*, 2018, 5, 946

# Experimental and theoretical calculation investigation on efficient Pb(II) adsorption on etched $Ti_3AlC_2$ nanofibers and nanosheets†

Pengcheng Gu,[a] Jinlu Xing,[a] Tao Wen,*[a] Rui Zhang,[a] Jian Wang,[a] Guixia Zhao,[a] Tasawar Hayat,[bc] Yuejie Ai,*[a] Zhang Lin[d] and Xiangke Wang*[abe]

Received 7th January 2018,
Accepted 13th February 2018

DOI: 10.1039/c8en00029h

rsc.li/es-nano

Layered 2D etched $Ti_3AlC_2$ nanofibers and nanosheets with different morphologies (named as e-TACFs and e-TACSs) were successfully synthesized by a simple hydrothermal treatment. The adsorption of Pb(II) on e-TACFs and e-TACSs under various conditions was found to be strongly dependent on pH and ionic strength. Thermodynamic parameters calculated from temperature-dependent isotherms showed that the adsorption of Pb(II) on both samples was spontaneous and endothermic. Specifically, due to their enhanced specific surface area and complexation affinity with Pb(II), the maximum adsorption capacity of Pb(II) on e-TACFs at pH 5.0 was 285.9 mg $g^{-1}$, which was higher than that of Pb(II) on e-TACSs (218.3 mg $g^{-1}$). The interaction mechanisms of Pb(II) with e-TACFs and e-TACSs were mainly attributed to cation exchange and outer-sphere surface complexation, which synergistically promoted the adsorption kinetics and enhanced the adsorption capacity. The DFT computational results were in good agreement with the batch experimental observations. Such a fluoride-free hydrothermal synthesis method and excellent heavy metal removal capacity demonstrate that 2D etched $Ti_3AlC_2$ nanomaterials are promising materials for the efficient removal of Pb(II) in environmental pollution remediation.

### Environmental significance

Lead (Pb), one of the most toxic metal ions, has aroused worldwide concern due to its high toxicity and carcinogenicity. Two-dimensional (2D) MXene materials exhibit not only hydrophilic surfaces but also excellent structure characteristics and chemical stabilities and are widely applied in the water decontamination field. This work evaluates the adsorption behavior of Pb(II) ions on etched $Ti_3AlC_2$ nanofibers and nanosheets, which are synthesized by an environmentally friendly fluoride-free treatment. The findings highlight the fluoride-free production of well-structured etched $Ti_3AlC_2$ and open a new perspective for the preparation of other functional 2D MXene materials for environmental pollution clean-up.

## Introduction

With the rapid development and operation of modern industry, environmental ecosystems and the health of human beings are seriously threatened by heavy metal pollution due to their high toxicity and carcinogenicity.[1–3] Lead (Pb) has been regarded as one of the most toxic metal ions which could cause nervous system damage and functional degradation of neurons even at trace concentrations.[4–6] In China, over 150 tons of Pb(II) are discharged into aqueous systems per year.[7] Considering its hazardous impact on the ecological environment and bioorganisms, developing an effective technology to remedy Pb(II)-bearing wastewater is of great practical importance.

Over the past few years, significant advances have been applied in Pb(II) pollution treatment with the development of various techniques, including adsorption,[8–10] membrane filtration,[11] chemical precipitation,[12] and so on. Specifically, the adsorption method has been widely applied to heavy metal ion clean-up by virtue of its low cost, high efficiency and easy operation.[13] Two-dimensional (2D) materials, such as graphene oxide and its derivatives which guarantee unique

[a] College of Environmental Science and Engineering, North China Electric Power University, Beijing 102206, P.R. China. E-mail: twen@ncepu.edu.cn, aiyuejie314@126.com, xkwang@ncepu.edu.cn; Fax: +86 10 61772890; Tel: +86 10 61772890
[b] NAAM Research Group, Faculty of Science, King Abdulaziz University, Jeddah 21589, Saudi Arabia
[c] Department of Mathematics, Quaid-I-Azam University, Islamabad 44000, Pakistan
[d] School of Environment and Energy, South China University of Technology, Guangzhou, 510006, P.R. China
[e] Collaborative Innovation Center of Radiation Medicine of Jiangsu Higher Education Institutions, School for Radiological and Interdisciplinary Sciences, Soochow University, Suzhou 215123, P.R. China

† Electronic supplementary information (ESI) available. See DOI: 10.1039/c8en00029h

morphologies, chemical structures and excellent adsorption capacities, have attracted multidisciplinary considerable attention. Zhao *et al.*[14] reported few-layered graphene oxide nanosheets as remarkable adsorbents for the removal of Cd(II) and Co(II) ions. Furthermore, graphene oxide-supported polyaniline composites were successfully synthesized and they showed high efficiency in removing radionuclides.[15] Unfortunately, the polydispersity of graphene oxide causes a real problem to its large scale application in wastewater remediation and becomes the prime challenge throughout the world.

Nowadays, a new family of 2D materials with graphene-like morphology labeled "Mxene" has received special attention due to their unique structural characteristics and hydrophilic surface.[16,17] The most studied members of the "Mxene" family (*i.e.*, $Ti_3C_2T_x$) produced by extraction of the Al layers from the 3D precursor $Ti_3AlC_2$ using hydrofluoric acid (HF) have found widespread applications in lithium-ion batteries,[18] supercapacitors,[19] and catalysts.[20] Meanwhile, benefiting from its unique layered structure and abundant hydroxyl functional groups, exfoliated $Ti_3C_2T_x$ exhibits superior adsorption performance. Ying and coworkers[21] reported 2D $Ti_3C_2T_x$ (T = OH or F) as a novel adsorbent for toxic Cr(VI) with high efficiency. In addition, $Ti_3C_2T_x$ nanosheets also showed an outstanding adsorption capacity for Ba(II) (9.3 mg $g^{-1}$) because of the formation of barium hydroxide or barium fluoride between the surface functional groups (introduced by exfoliation using HF) and Ba(II) ions.[22] To date, the hydrofluoric acid etching method is the most used strategy with respect to the strong metallic and covalent bonds among the layers.[23] However, the high toxicity of procedures involving fluoride to the environment somehow restricts its scope of potential applications. Therefore, developing an effective fluoride-free method towards the synthesis of a well-layered structured and functionalized $Ti_3AlC_2$ is technologically important for wastewater purification.

Herein, we studied the structural evolution of $Ti_3AlC_2$ by etching Al layers *via* a facile hydrothermal alkaline reaction (Scheme 1). Interestingly, two different morphologies of nanofibers and nanosheets were obtained using varying alkaline medium solution concentrations (5 M NaOH for e-TACFs and 15 M NaOH for e-TACSs). By modifying the pristine $Ti_3AlC_2$ with this facile method, multi-functional oxygen-containing groups were introduced without the risk of fluorine pollution. Thus, the increased functional groups together with the enhanced specific surface area make the as-prepared nanomaterials an ideal platform for environmental pollution clean-up. In consideration of the perniciousness of heavy metal ions, Pb(II) was selected as the representative potentially toxic metal ion to evaluate the adsorption ability of the etched $Ti_3AlC_2$ nanomaterials. The adsorption mechanisms of Pb(II) on e-TACFs and e-TACSs were investigated by conducting various batch experiments under different conditions (*i.e.*, pH, ionic strength, contact time, temperature and spectroscopy). This study provides a "green" approach for fabricating 2D layered materials and broadens their applicability in wastewater clean-up.

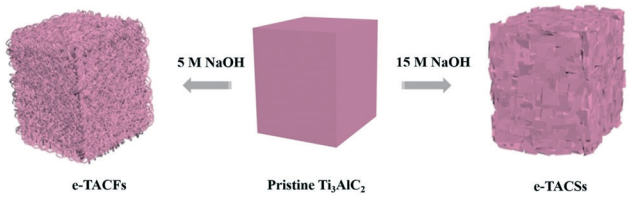


Scheme 1 Schematic of formation of etched $Ti_3AlC_2$ (nanosheets and nanofibers).

## Materials and methods

### Preparation of e-TAC nanostructures

All chemical reagents were purchased from Sinopharm Chemical Reagent Co. (China). $Ti_3AlC_2$ powders (~98% purity), sodium hydroxide (NaOH), sodium nitrate ($NaNO_3$), nitric acid ($HNO_3$) and Milli-Q water (18.2 MΩ $cm^{-1}$) were used in the experiments. 100 mg $Ti_3AlC_2$ powders were dispersed and immersed in 40 mL 5 M (8.0 g) and 15 M (24.0 g) NaOH solutions, respectively. After successive magnetic stirring for 1 h, the resulting homogeneous suspensions were transferred into a 50 mL Teflon-lined stainless steel autoclave and then hydrothermally treated at 200 °C for 12 hours. After cooling them down naturally to room temperature, the acquired sediments were collected through centrifugation at 8000 rpm for 10 min. Using a centrifugation-redispersion method, the sediments were washed with ethanol and deionized water ten times until a neutral pH value was achieved. The final products were dried in a vacuum at 60 °C for 20 h.

### Physicochemical characterization

The microstructures and morphologies of the pristine $Ti_3AlC_2$, as-prepared e-TACFs and e-TACSs were characterized using a scanning electron microscope (SEM, Hitachi S-4800) operated at a beam energy of 5 kV. TEM imaging and X-ray spectroscopy elemental mapping analyses were performed using a JEOL-2010 microscope with an accelerating voltage of 200 kV. The X-ray diffraction (XRD) data pattern was recorded on a diffractometer with Cu-Kα radiation ($\lambda$ = 1.5418 Å) with a scanning speed of 3° $min^{-1}$. Raman spectroscopy was carried out using an inVia microscope with a confocal Raman spectrometer (Horiba) using a 532 nm laser beam. X-ray photoelectron spectroscopy (XPS) spectra were measured using a VG Scientific ESCALAB Mark II spectrometer, which was equipped with two ultrahigh vacuum (UHV) chambers. The pore size distribution and Brunauer–Emmett–Teller (BET) surface area were obtained by using a Micromeritics ASAP 2010 system at 77 K. Zeta potential values were measured using a ZETASIZER 3000 HSA system.

### Adsorption experiments

The adsorption experiments were performed by using a batch technique in polyethylene centrifuge tubes. The stock aqueous suspensions of e-TACFs and e-TACSs (1.2 g $L^{-1}$), $NaNO_3$

(1 M) and Pb(II) (200 mg $L^{-1}$) were added into the tubes to achieve the desired concentrations of various components. A negligible volume of 0.1 M/0.01 M $HNO_3$ or NaOH solution was used to adjust the pH of the mixture. The mixture suspension was shaken for 24 h to ensure adsorption equilibrium and the solid phase was separated from the liquid phase by centrifugation at 10 000 rpm for 10 min. The concentration of Pb(II) in the supernatant was determined by inductively coupled plasma (ICP) spectroscopy. The amounts of adsorbed Pb(II) ($q_e$) were calculated from the variance between the initial concentration $C_0$ (mg $L^{-1}$) and the equilibrium concentration $C_e$ (mg $L^{-1}$) in the supernatant after separation, which was derived from eqn (1), and the adsorption (%) was calculated using eqn (2).

$$q_e = \frac{V \times (C_0 - C_e)}{m} \quad (1)$$

$$\text{Adsorption}\% = \frac{(C_0 - C_e)}{C_0} \times 100\% \quad (2)$$

where $m$ (mg) and $V$ (mL) represent the dosage of the adsorbent and the total volume of the suspension, respectively.

### DFT computational details

Periodic plane-wave-based DFT calculations have been performed by using the standard projector augmented wave (PAW) potentials which were incorporated into the Vienna *ab initio* simulation package (VASP) code.[24,25] In the present work, the generalized gradient approximation (GGA) with the Perdew–Burke–Ernzerhof (PBE) functional was applied to the exchange correlation.[25] The kinetic cut-off energy was considered to be 500 eV. The convergence criteria for energy and force were set at $10^{-5}$ eV and 0.01 eV $Å^{-1}$, respectively. The $k$-point mesh of 4 × 4 × 1 within the Monkhorst–Pack scheme was chosen to sample the Brillouin zone.[26]

## Results and discussion

### Characterization

Microstructure characterization. The typical SEM and TEM images of the as-prepared e-TACFs and e-TACSs are illustrated in Fig. 1. The pristine $Ti_3AlC_2$ showed the typical characteristic of a 3D bulk structure with a random surface and an irregular edge (Fig. S1†). After being hydrothermally treated with 5 M NaOH, the pristine $Ti_3AlC_2$ was converted into nanofiber structures (labeled e-TACFs) with an average size of approximately 1 μm (Fig. 1a and c). Meanwhile, nanosheets with a smooth surface and a regular edge (denoted as e-TACSs) were formed in 15 M NaOH (Fig. 1b and d). The morphology evolution of the pristine $Ti_3AlC_2$ confirmed the successful modification on the surface. In order to identify their composition and inner architectures, the spatial distribution of different elements in e-TACFs and e-TACS was measured by elemental mapping. The EDX results (Fig. 2) revealed that the component elements Ti, Na, C and O were homogeneously distributed over the nano-sized structure surfaces. However, the presence of partially dispersed Al element was observed, which might come from the etching of Al between the layers.

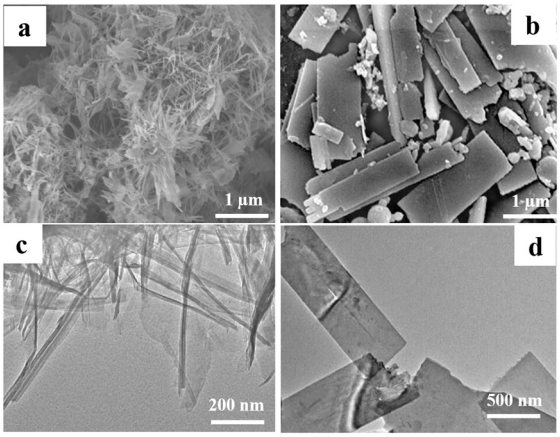


Fig. 1 SEM images of e-TACSs (a) and e-TACFs (b); TEM images of e-TACSs (c) and e-TACFs (d).

The crystallographic structures of the pristine $Ti_3AlC_2$ and the post-etching samples were characterized by XRD. As shown in Fig. 3a, the diffraction peaks at 9.62°, 19.2°, 34.6° and 39.0° correspond to the typical representation of $Ti_3AlC_2$ crystal phases.[29] Notably, the typical representative peak intensities were obviously lower than those of the pristine $Ti_3AlC_2$ after the alkaline immersion treatment, suggesting a slight decrease in the degree of crystallinity. The XRD patterns of the resulting e-TACFs and e-TACS clearly revealed that the intensity of the (104) peak at 39.0° became weak (Fig. S2†), indicating the partial extraction of Al species, which was consistent with the result of EDX element mapping. However, the Al signal peaks manifested the residual

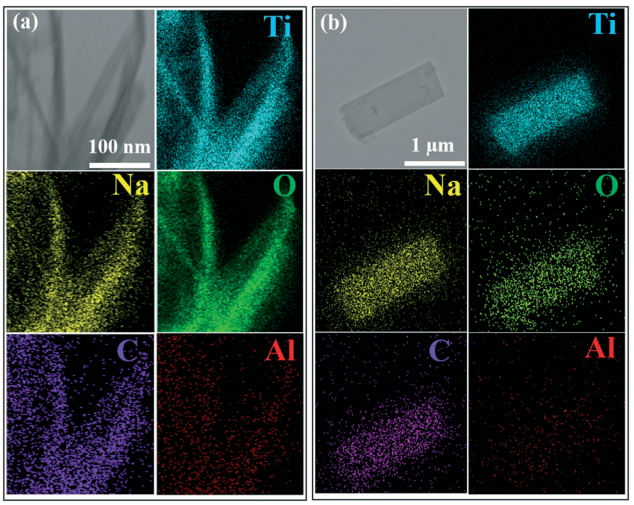


Fig. 2 Elemental mapping images of Ti, Na, O, C, and Al for e-TACFs (a) and e-TACSs (b).

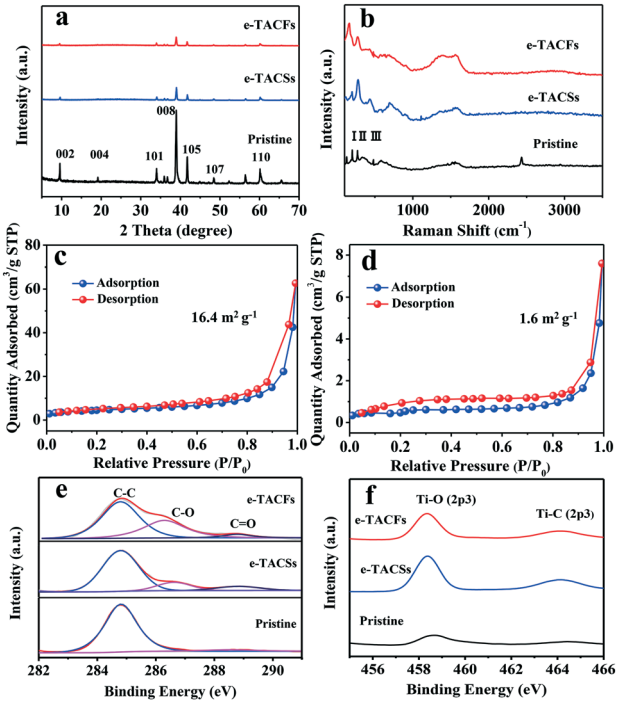


**Fig. 3** (a) XRD patterns of pristine $Ti_3AlC_2$, e-TACFs and e-TACSs; (b) Raman spectra of pristine $Ti_3AlC_2$, e-TACFs and e-TACSs; $N_2$ adsorption–desorption isotherms of e-TACFs (c) and e-TACSs (d); XPS spectra of C 1s (e) and O 1s (f) of pristine $Ti_3AlC_2$, e-TACFs and e-TACSs.

traces of Al species in the layered structure due to the strong chemical bonds existing in the $Ti_3AlC_2$ phase. The Raman spectra of $Ti_3AlC_2$ before and after NaOH treatment are shown in Fig. 3b. Peaks I, II, and III are assigned to the merged, broadened and shifted vibrations of Al–Ti, respectively.[27] The broadened and shifted peaks confirmed the destruction of Al–Ti bonding after etching. This phenomenon is in good agreement with the weakened XRD profiles.

The $N_2$ adsorption–desorption isotherms of e-TACFs and e-TACSs are shown in Fig. 3c and d. According to BET measurements, the specific surface areas of the nanofibers and nanosheets were calculated to be 16.4 $m^2\ g^{-1}$ and 1.6 $m^2\ g^{-1}$, respectively, which were higher than that of pristine $Ti_3AlC_2$ (1.2 $m^2\ g^{-1}$),[28] further confirming the evolution of the structure and morphology. Therefore, the difference between the specific surface areas of e-TACFs and e-TACSs can significantly influence their performance in pollution management.

Further details about the chemical structures of the surface were characterized by XPS. The XPS spectra revealed that titanium (Ti), aluminum (Al), and carbon (C) were the predominant elements on the surface of $Ti_3AlC_2$. Compared with the pristine $Ti_3AlC_2$, an apparent decrease in Al 2p intensity and the appearance of a distinct Na 1s peak were recorded from the e-TACF and e-TACS samples (Fig. S3†), demonstrating the successful removal of the Al component and introduction of $Na^+$ during the alkalization process.[29] The specific surface elemental contents of the pristine $Ti_3AlC_2$, e-TACFs, and e-TACSs are summarized in Table S1.† It was found that the oxygen contents of e-TACF and e-TACS samples sharply increased. In other words, after the alkaline treatment, abundant oxygen-containing functional groups were incorporated into the layered nanostructures, which would provide plentiful binding sites for the target ions. As shown in Fig. 3e, the C 1s spectrum of $Ti_3AlC_2$ can be divided into three components: C–C (~284.4 eV), C–O (286.6 eV), and C═O bonding (288.8 eV). After alkaline treatment, the relatively strong C–O and C═O bonding appeared in the C 1s spectra of e-TACFs and e-TACSs, indicating the formation of $Ti_3C_2(OH)_2$.[21,30] From the high resolution Ti 2p spectra, the predominant peaks of Ti–O (2p3) and Ti–C (2p3) bonds were evidently observed.[31] The fact that the intensities of Ti–C and Ti–O bonds were enhanced further confirmed the formation of $Ti_3C_2(OH)_2$ on the surfaces of e-TACFs and e-TACSs. Such a phenomenon was reported by a previous report as well.[23]

The FT-IR spectroscopy technique was carried out to have a better understanding of the variation of functional groups (Fig. S4†). The absorption peaks of pristine $Ti_3AlC_2$ at 500–700 $cm^{-1}$ could be assigned to the deformation vibration of the Ti–O bond. The sharp peaks at ~1632 and ~3418 $cm^{-1}$ were ascribed to the strongly bound $H_2O$ and –OH.[29] Obviously, a new peak near 904 $cm^{-1}$ was observed in the etched products, which was ascribed to the vibration of Ti–$O(ONa)_2$.[32] The transformation of the bonding characteristics of $Ti_3AlC_2$ before and after etching further confirmed the successful surface modification.

Based on the above results, it was clear that the $Ti_3AlC_2$ structure successfully evolved during the rapid alkalization treatment. This strategy resulted in the surface etching of Al from the bulk $Ti_3AlC_2$ and the formation of $Ti_3C_2$ covered with a mixture of functional groups (–ONa and –OH) (Scheme 2). The activation mechanism between alkali hydroxide and $Ti_3AlC_2$ might be expressed by the following reactions:

$$Ti_3AlC_2 + (1 - x)NaOH + H_2O = Ti_3Al_xC_2 + (1 - x)NaAlO_2 + 3/2(1 - x) + H_2\uparrow \quad (a)$$

$$Ti_3Al_xC_2 + 2H_2O = Ti_3Al_xC_2(OH)_2 + H_2\uparrow \quad (b)$$

$$Ti_3Al_xC_2 + 2NaOH = Ti_3Al_xC_2(ONa)_2 + H_2\uparrow \quad (c)$$

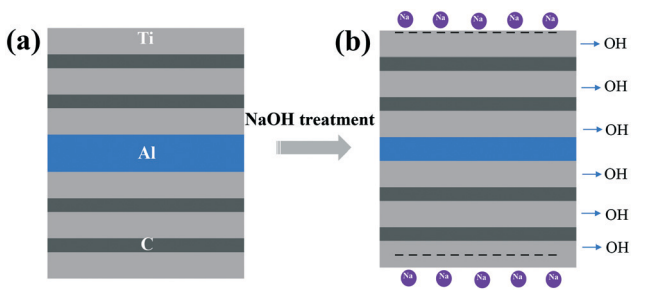


**Scheme 2** Schematic of the etching process of $Ti_3AlC_2$: (a) $Ti_3AlC_2$ structure; (b) etching Al from bulk $Ti_3AlC_2$ and introduction of –ONa and –OH after reaction with NaOH.

### Adsorption capacity studies

The adsorption isotherms of Pb(II) on e-TACSs and e-TACFs were obtained under three different temperatures at pH 5.0. As shown in Fig. 4a and b, the maximum values ($Q_e$) increased along with the temperature (*i.e.*, 298 K < 313 K < 328 K), indicating that a higher temperature was preferred by the Pb(II) adsorption. Langmuir and Freundlich models were applied to simulate the adsorption isotherms, which are presented as:[33]

$$\text{Langmuir model:}\quad q_e = \frac{K_L Q_{max} C_e}{1 + K_L C_e} \tag{3}$$

$$\text{Freundlich model:}\quad Q_e = K_f C_e^{1/n} \tag{4}$$

where $Q_e$ (mg $g^{-1}$) is the amount of Pb(II) adsorbed on the solid phase, $C_e$ (mg $L^{-1}$) is the equilibrium concentration of Pb(II), $Q_{max}$ is the adsorption capacity after equilibration (mg $g^{-1}$), $b$ (L $mol^{-1}$) is a constant related to the adsorption heat, $K_f$ (mg $g^{-1}$) represents the adsorption capacity when the equilibrium concentration is equal to 1 and $n$ is the degree of adsorption dependence.

The parameters calculated from the two models are listed in Table 1. From the regression coefficients ($R^2$), the Langmuir model displayed a preferable fitting result compared to the Freundlich model, suggesting the homogeneous distribution of active sites on e-TACSs and e-TACFs.[34] In comparison, the maximum values ($Q_{max}$) of Pb(II) adsorption on e-TACFs were much higher than those of Pb(II) on e-TACSs. For instance, the $Q_{max}$ values of Pb(II) on e-TACFs and e-TACSs calculated from the Langmuir model at pH 5.0 and 298 K were 285.9 mg $g^{-1}$ and 218.3 mg $g^{-1}$, respectively. The higher $Q_{max}$ of Pb(II) on e-TACFs can be ascribed to the higher surface area and the abundant oxygen-containing functional groups, which synergistically promoted the Pb(II) adsorption. Compared with previous reports, the adsorption of Pb(II) (Table S2†) on e-TACFs and e-TACSs exhibited a higher adsorption capacity than on many other materials. Thus, the studied samples etched from $Ti_3AlC_2$ were suitable materials for the efficient removal of Pb(II) from aqueous solutions.

In order to investigate the thermodynamic feasibility of the adsorption process, the thermodynamic parameters (*i.e.*, standard free energy change $\Delta G^0$, standard enthalpy change $\Delta H^0$, and standard entropy change $\Delta S^0$) were calculated from the temperature-dependent adsorption isotherms (Fig. S5†). The thermodynamic parameters were derived from the plots of $\ln K^0$ *vs.* $1/T$ using the following equations:[35]

$$\Delta G^0 = -RT \ln K^0 \tag{5}$$

$$\ln K^0 = \frac{\Delta S^0}{R} - \frac{\Delta H^0}{RT} \tag{6}$$

where $K^0$ represents the adsorption equilibrium constant, $T$ is the absolute temperature in Kelvin and $R$ (8.314 J $mol^{-1}$ $K^{-1}$) is the gas constant.

The thermodynamic values calculated from eqn (5) and (6) at different temperatures are tabulated in Table 2. The positive $\Delta H^0$ values of 15.26 kJ $mol^{-1}$ for e-TACFs and 8.84 kJ $mol^{-1}$ for e-TACSs revealed that the adsorption process was endothermic. In addition, the positive $\Delta S^0$ values confirmed the feasibility and high affinity of Pb(II) on e-TACFs and e-TACSs. The negative $\Delta G^0$ values also indicated the spontaneous nature of the adsorption process, and the $\Delta G^0$ values of Pb(II) on e-TACFs were more negative than those of Pb(II) on e-TACSs, suggesting that the adsorption on e-TACFs was more spontaneous than that of Pb(II) on e-TACSs. The thermodynamic parameters reflected that both samples exhibited excellent adsorption potential towards Pb(II) in aqueous solutions.

In order to evaluate the adsorption performances of etched $Ti_3AlC_2$ products in a real water environment, we further examined the treatment capacity of etched $Ti_3AlC_2$ nanofibers in simulated lead-spiked drinking water. As illustrated in Fig. 4c, e-TACFs presented an outstanding Pb(II) adsorption performance and the average water treatment capacity is 2500 kg of water per kg of e-TACFs. The value of the Pb(II) content in the effluent was approximately 8 μg $L^{-1}$, which meets the drinking water standard recommended by the World Health Organization (10 μg $L^{-1}$). The free-standing e-TACF membrane can be further used as an adsorbent for advanced Pb(II)-contained water treatment (Fig. S6†). The experimental results show that e-TACFs and e-TACSs are suitable adsorbents for the decontamination of Pb(II) for simulated lead-contaminated drinking wastewater. Moreover, their outstanding properties in solid–liquid separation during the Pb(II) removal process were observed in a short time (20 min), which is definitely beneficial to their potential applications (Fig. S7†).

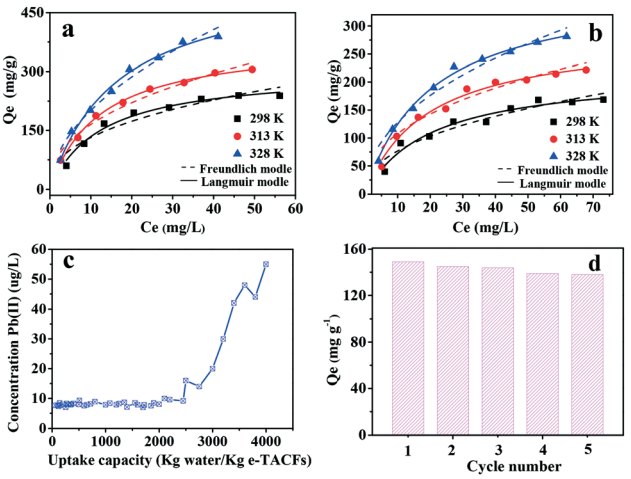


**Fig. 4** The adsorption isotherms of Pb(II) on e-TACFs (a) and e-TACSs (b) obtained at different temperatures. Conditions: pH = 5.0 ± 0.1, $m/V$ = 0.1 g $L^{-1}$, and $I$ = 0.01 M $NaNO_3$. (c) Treatment capacity of e-TACFs for simulated drinking water containing Pb(II) ions with an initial concentration of 100 μg $L^{-1}$. Conditions: Ca(II) = 40 mg $L^{-1}$, Mg(II) = 80 mg $L^{-1}$, Na(I) =100 mg $L^{-1}$, and pH = 6.8–7.2. (d) Recycling of e-TACFs for the removal of Pb(II) ions. pH = 5.0 ± 0.1, $C(Pb)_{initial}$ = 20 mg $L^{-1}$, $m/V$ = 0.1 g $L^{-1}$, $I$ = 0.01 M $NaNO_3$ and $T$ = 298 K.

Table 1 Parameters calculated from the Langmuir and Freundlich models

| | | e-TACFs | | | e-TACSs | | |
|---|---|---|---|---|---|---|---|
| Adsorbents | Parameters | 298 K | 313 K | 328 K | 298 K | 313 K | 328 K |
| Langmuir | $Q_e$ (mg g$^{-1}$) | 285.9 | 380.3 | 549.1 | 218.3 | 286.2 | 373.3 |
| | $R^2$ | 0.98 | 0.99 | 0.99 | 0.95 | 0.98 | 0.99 |
| Freundlich | 1/*n*F | 0.39 | 0.41 | 0.50 | 0.43 | 0.43 | 0.46 |
| | $R^2$ | 0.89 | 0.96 | 0.97 | 0.91 | 0.92 | 0.95 |

## Regeneration

Considering feasibility and economic efficiency, the cycling performance of e-TACFs was explored through adsorption–desorption cycles. As shown in Fig. 4d, the adsorption capacity of e-TACFs decreased from 147.5 mg g$^{-1}$ to 141.5 mg g$^{-1}$ for Pb(II) after five cycles of the regeneration/reuse process, suggesting that e-TACFs exhibit excellent utilization for long-term usage.

## Kinetics studies

Kinetics experiments were performed to evaluate the adsorption rates of Pb(II) on as-etched $Ti_3AlC_2$. Fig. 5 shows the Pb(II) adsorption curves of e-TACFs and e-TACSs under different contact times. It was clear that Pb(II) adsorption occurred in two distinct steps: a relatively fast adsorption step followed by a slow uptake tendency until equilibrium. The adsorption capacities of Pb(II) on e-TACFs and e-TACSs were 164.8 mg g$^{-1}$ and 145.3 mg g$^{-1}$ within the initial contact time of 120 min, whereas only small amounts of Pb(II) were further adsorbed on e-TACFs (2.5 mg g$^{-1}$) and e-TACSs (8.1 mg g$^{-1}$) in the following reaction time. The occurrence of a rapid adsorption step can be attributed to numerous binding sites at the solid particle surfaces, and then the active binding sites on the surface of e-TACFs and e-TACSs were gradually occupied by Pb(II) ions, which resulted in a slower adsorption step.[36]

To study the underlying adsorption kinetics in detail, the pseudo-first-order model and pseudo-second order model were exploited to simulate the experimental data. The kinetic models are presented as follows:[37]

$$\ln(q_e - q_t) = \ln q_e - k_1 t \quad (7)$$

$$\frac{t}{q_t} = \frac{1}{k_2 q_e^2} + \frac{t}{q_e} \quad (8)$$

where $k_1$ (min$^{-1}$) and $k_2$ (g mg$^{-1}$ min$^{-1}$) represent the rate constant of the pseudo-first order and pseudo-second order models, respectively. $q_t$ (mg g$^{-1}$) and $q_e$ (mg g$^{-1}$) refer to the adsorption capacity at time $t$ (min) and the amount of Pb(II) adsorbed at equilibrium, respectively.

The $k_1$ and $q_e$ values of the pseudo-first order model were obtained from the linear plot of ln ($q_e - q_t$) *versus* $t$ (min) (figure not shown). Meanwhile, the plot of $t/q_t$ *versus* $t$ (min) was linear fitted to calculate the pseudo-second order correlation parameters (insets of Fig. 5a and b). According to the correlation coefficients ($R^2$) from Table S3,† it can be concluded that the pseudo-second order model fitted the kinetic data better than the pseudo-first order model. Moreover, the $k_2$ of Pb(II) adsorption on e-TACFs was 5.8 × 10$^{-3}$ g mg$^{-1}$ min$^{-1}$, which was much higher than that on e-TACSs ($k_2$ = 1.1 × 10$^{-3}$ g mg$^{-1}$ min$^{-1}$), indicating that the adsorption of Pb(II) on e-TACFs was faster than that of Pb(II) on e-TACSs. This phenomenon further suggested that the rate determining mechanism for Pb(II) adsorption on e-TACSs and e-TACFs was the chemisorption.

## Effect of pH and ionic strength

Generally, the pH value and the ionic strength play a critical role in the migration and transformation behavior of heavy metal ions. Thus, the effects of pH and ionic strength were studied to investigate the adsorption mechanism. As illustrated in Fig. 6, it can be seen that the solution pH displayed a significant influence on the adsorption of Pb(II) onto e-TACSs and e-TACFs, which could be divided into three regions (Fig. 6a and b). Specifically, the adsorption of Pb(II) on e-TACSs and e-TACFs increased gradually as the pH increased from 2.0 to 7.0, and maintained a high level in the pH range of 7.0–9.5. Subsequently, the removal percentage declined at pH > 9.5. The adsorption process was proposed to be greatly

Table 2 Thermodynamic parameters for Pb(II) adsorption on e-TACFs and e-TACSs

| Parameters | $\Delta H^0$ (kJ mol$^{-1}$) | $\Delta S^0$ (J mol$^{-1}$ K$^{-1}$) | $\Delta G^0$ (kJ mol$^{-1}$) | | |
|---|---|---|---|---|---|
| Adsorbents | | | 298 K | 313 K | 328 K |
| e-TACFs | 15.26 | 74.6 | −6.94 | −8.31 | −9.56 |
| e-TACSs | 8.84 | 48.8 | −5.22 | −6.32 | −7.28 |

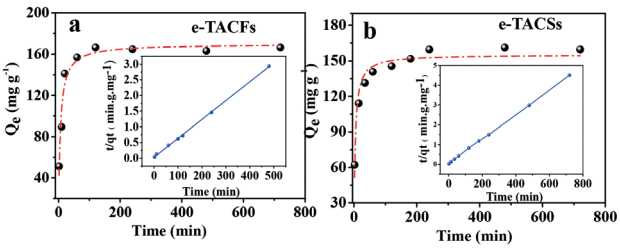


Fig. 5 The time-dependent adsorption of Pb(II) on e-TACFs (a) and e-TACSs (b). Conditions: pH = 5.0 ± 0.1, $C(Pb)_{initial}$ = 20 mg L$^{-1}$, $m/V$ = 0.1 g L$^{-1}$, $I$ = 0.01 M and T = 298 K. The inserted curves are the pseudo-second order kinetic plots of Pb(II) adsorption on e-TACFs and e-TACSs.

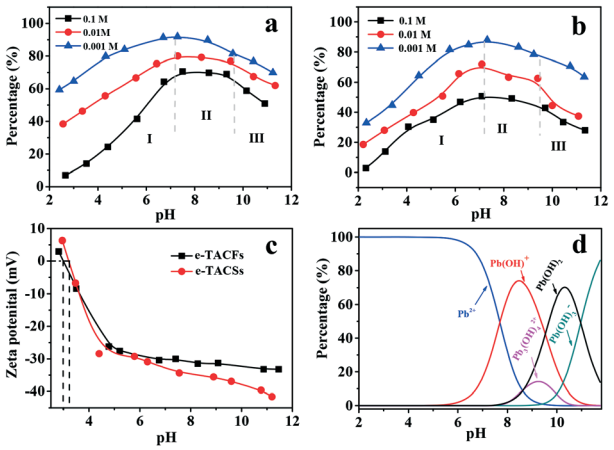


Fig. 6 Effect of pH and ionic strength on Pb(II) adsorption on e-TACFs (a) and e-TACSs (b); conditions: $C(Pb)_{initial}$ = 20 mg $L^{-1}$, $m/V$ = 0.1 g $L^{-1}$, $I$ = 0.1 M, 0.01 M, 0.001 M and $T$ = 298 K, (c) zeta potential of e-TACFs and e-TACSs, and (d) relative distribution of Pb(II) species under different pH values. Conditions: $C(Pb)_{initial}$ = 20 mg $L^{-1}$.

affected by both the existent form of the adsorbate and the surface property of the adsorbent. Thus, the zeta potentials of the as-prepared products and the species distribution of aqueous Pb(II) were further studied. At pH < $pH_{PZC}$, the strong electrostatic repulsion and the competition with $H^+$ were the main constraints for the adsorption of $Pb^{2+}$. As the pH increased from $pH_{PZC}$ to 7.0, the negatively charged surface and the reduced competition with $H^+$ can facilitate the effective interaction of $Pb^{2+}$ with e-TACFs and e-TACSs, leading to a remarkable increase in the removal percentage. In the pH range of 7.0–9.5, the adsorption was mainly controlled by the ion-exchange between $[Ti–O]^-Na^+$ and $Pb^{2+}$ or $Pb(OH)^+$ (ref. 38 and 39) because of the ignorable competition effect of $H^+$. As a result, the removal percentage was strongly dependent on pH and thereby maintained at a high level. At pH > 9.5, the $Pb(OH)_2$ and $Pb(OH)_3^-$ species were formed and difficult to adsorb on the negatively charged solid, resulting in a negative effect on the ion exchange reaction, which was the main reason for the reduction of removal percentage. Considering the realistic lead-containing effluent, we further investigated the effect of solid content on adsorption percentage under acidic conditions. As illustrated in Fig. S8,† the adsorption percentage increased from 60.2% to 92.9% as the e-TACFs content increased from 0.1 g $L^{-1}$ to 1.0 g $L^{-1}$ even at pH = 2.0, demonstrating their potential application in Pb(II) wastewater disposal.

The effect of ionic strength on Pb(II) adsorption onto e-TACSs and e-TACFs was investigated in 0.001, 0.01, and 0.1 M $NaNO_3$ solutions, respectively. As shown in Fig. 6a and b, it was found that the adsorption of Pb(II) on both samples was remarkably dependent on ionic strength. The uptake percentage of Pb(II) displayed an increasing tendency with the decrease in salt concentration at the experimental pH values, which demonstrated that the adsorption process might be dominated by ion exchange or outer-sphere surface complexation.[40] As the ionic strength decreased, the available active sites for Pb(II) increased due to the weak competition between $Na^+$ and Pb(II). This may be explained by the following reasons: firstly, the activity coefficient of Pb(II) was negatively affected by the enhanced ionic strength, which restricted the movement from the solution to the solid surfaces.[41,42] Secondly, the solid particles tended to aggregate together at high ionic strength, which largely lowered the amount of potential binding sites for ion exchange and thereby diminished the adsorption of Pb(II) on e-TACFs and e-TACSs.[43] Finally, the amplified electrical double layer thickness subdued the electrostatic attraction, and thereby reduced the Pb(II) adsorption on e-TACFs and e-TACSs at a high salt concentration.[44] Thus, the interaction mechanisms can be described by ion-exchange reaction accompanied by outer-sphere surface complexation. On the basis of the above discussion, the as-etched samples are considered to be promising materials for Pb(II) removal from wastewater due to their excellent ion exchange performance in a wide pH range.

## Nanomaterial–pollutant interaction mechanism

### Zeta potential and XPS analysis

The interaction mechanism between Pb(II) and e-TAC was investigated by zeta potential and XPS analysis. As illustrated in Fig. 6c, the $pH_{PZC}$ (point of zero charge) values of e-TACFs and e-TACSs were approximately 3.0. The zeta potential of the samples could explain the highly efficient capture of Pb(II) at pH > $pH_{PZC}$. Obviously, the electrostatic attraction provided driving forces to facilitate the diffusion of Pb(II) ions from solution to e-TACF and e-TACS solids.

The XPS technique was further introduced for the characterization of the samples before (denoted as e-TACSs and e-TACFs) and after adsorption (denoted as e-TACSs-Pb and e-TACFs-Pb), and the corresponding results of surface element analyses are listed in Table S4.† As shown in the XPS wide scan survey (Fig. 7a), the dramatic decrease in Na 1s peaks after adsorption was accompanied by the appearance of Pb 4f peaks, which reasonably indicated that ion exchange between $Pb^{2+}$ and $Na^+$ might be the major adsorption mechanism (Fig. 7b and c). The high-resolution spectra of Pb 4f were obtained to investigate the chemical state of the adsorbed Pb(II). It was found that the binding energy of Pb $4f_{7/2}$ was centered at 139.1 eV, which was lower than that of $Pb(NO_3)_2$ (139.5 eV),[45] indicating the strong interaction between the loaded $Pb^{2+}$ and the active sites.[28] The high-resolution O 1s spectra were also studied to reveal the bonding interaction between oxygen-containing groups and $Pb^{2+}$ (Fig. 7d and e). It can be seen that the O 1s spectra of e-TACFs and e-TACSs before Pb(II) adsorption displayed two peaks at 530.0 and 532.0 eV, which could be ascribed to the $[Ti–O]^-Na^+$ and Ti–OH surface sites, respectively.[30,46] After the loading of $Pb^{2+}$, the binding energy values of the two peaks of e-TACFs and e-TACSs remarkably shifted by 0.6 and 0.3 eV, respectively (summarized in Table S5†), which implied the alteration of the local bonding surroundings. Similar shifts were also

 

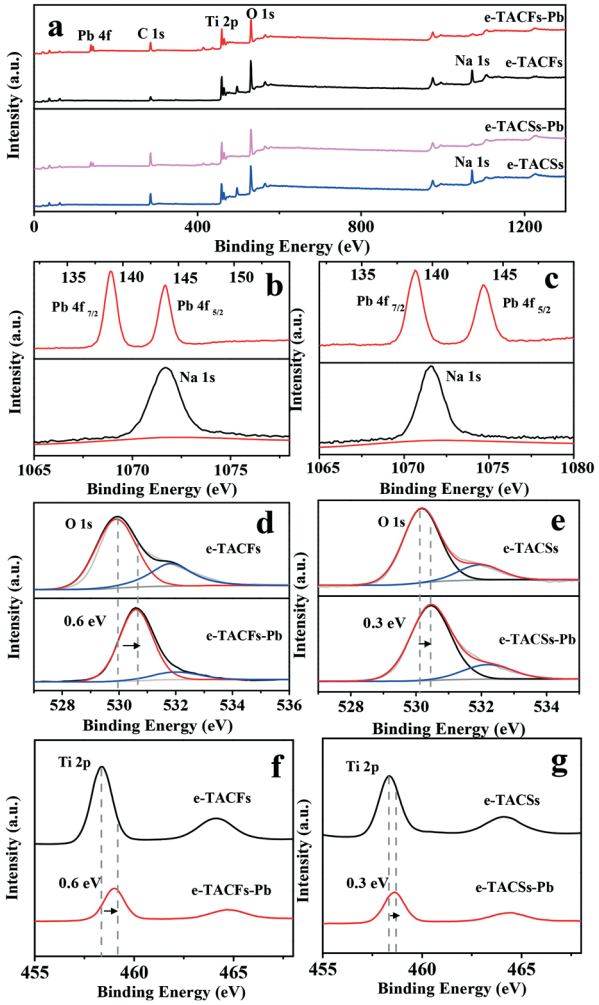


Fig. 7 (a) XPS spectra of e-TACFs and e-TACSs before and after Pb(II) adsorption; XPS spectra of Pb $4f_{5/2}$, Pb $4f_{7/2}$ and Na 1s of e-TACFs (b) and e-TACSs (c); O 1s of e-TACFs (d) and e-TACSs (e) before and after Pb(II) adsorption; Ti 2p of e-TACFs (f) and e-TACSs (g) before and after Pb(II) adsorption.

observed in the Ti 2p spectra, further demonstrating the strong complexation affinity of Ti–O surface sites with $Pb^{2+}$ ions.

It is well accepted that electrostatic attraction is the dominant interaction between the hydrated sodium ion $(Na^+(H_2O)_n)$ and the charged surface site $[\equiv Ti\text{–}O]^-$. Thus, the surface charge was distributed mainly on the O atom of $[\equiv Ti\text{–}O]^-$ sites. When $Pb^{2+}$ was adsorbed through the ion-exchange reaction with $Na^+(H_2O)_n$, the electron-rich orbitals of O 2p would hybridize with the empty orbitals of Pb 6p, leading to electron migration from O to Pb. After accepting the coordinated electron, the Pb nucleus would weaken its restriction on the electrons in the 4f orbits so that they are able to be excited by X-ray with lower energy. As a result, the photoelectron binding energy of the adsorbed Pb was red shifted. In contrast, the O nucleus will strengthen its restriction on the electrons in the 1s orbital so that their photoelectron binding energy was blue shifted. Furthermore, the complexation effect of oxygen would force the shared electrons of the Ti–O bond to move away from Ti, leading to a blue shift of the Ti 2p photoelectron binding energy. The same reason can be used to explain the changes in the ≡Ti–OH site. In addition, it was calculated that the area fraction of $[\equiv Ti\text{–}O]^-$ was much larger than that of ≡Ti–OH (Table S5†), indicating that ion-exchange reaction was the major mechanism while surface complexation reaction also made a certain contribution. Notably, it was easy to find that the bonding shift of e-TACFs (0.6 eV) was greater than that of e-TACFs (0.3 eV). Such a difference in bonding shift might be attributed to the stronger interaction force between Pb(II) and Ti–O of e-TACFs compared to that of e-TACSs, which was beneficial to the formation of strong surface complexes with Pb(II) which exhibited a superior adsorption capacity.

## DFT calculations

To gain a better insight into the structures and binding energies and understand the adsorption behavior between Pb(II) and e-TACFs or e-TACSs at the molecular level, geometric optimizations for Pb(II) adsorbed on the etched $Ti_3AlC_2$ have been carried out using periodic plane-wave-based DFT calculations. For the model construction, we built the $Ti_3AlC_2$ model based on the crystal structure of $Ti_3AlC_2$ whose space group is $P6_3/mmc$ (No.194); see Fig. 8a. The unit cell parameters are $a = b = 3.07530$ Å, $c = 18.57800$ Å, $\alpha = \beta = 90°$, and $\gamma = 120°$. According to the aforementioned results, a 2 × 2 super cell along the (0 0 1) surface with –OH functional groups was then established for the subsequent calculations. Since the adsorption process mainly occurred on the upper surface, therefore, considering the computational cost, the inner second layer was fixed during the geometric optimizations. To neutralize the positively charged $Pb^{2+}$, two nitrate ions were added into the system, as shown in Fig. 9a. The optimized structure for the Pb(II) adsorbed on the surface of $Ti_3AlC_2$ is depicted in Fig. 9b.

As shown in Fig. 9, Pb(II) formed a strong bond with the O atom on the surface, and the Pb–O bond length was

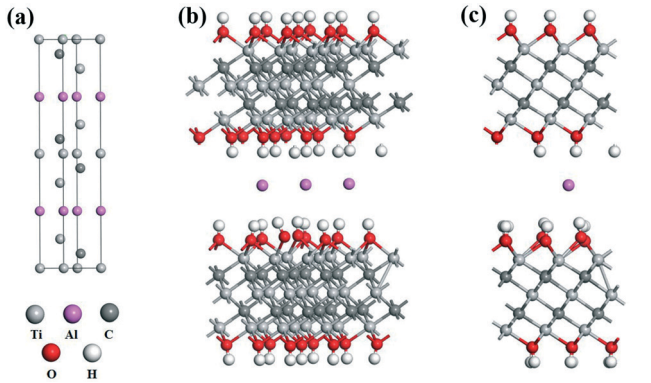


Fig. 8 (a) The unit cell for the crystal structure of $Ti_3AlC_2$. The optimized structure for the etched $Ti_3AlC_2$ from a side view (b) and a cross-sectional view (c).

calculated to be 2.550 Å. The binding energy of this process was then calculated to be 30.90 kcal $mol^{-1}$, which indicated a strong chemical adsorption behavior. The adsorption energy ($E_{ad}$) was measured according to the following formula: $E_{ad} = E_{Pb/X} - E_{(Pb+X)}$, where X represents the etched $Ti_3AlC_2$ and Pb/X represents the complex of Pb(II) adsorbed on the etched $Ti_3AlC_2$. The Pb+X system stands for the separated adsorbent X and the Pb ion, in which the ion is placed far away from the etched $Ti_3AlC_2$ surface to eliminate possible mutual interaction. Therefore, from a theoretical perspective, the Pb(II) ion was mainly interrelated with functional oxygen atoms on the surface and the etched $Ti_3AlC_2$ has a strong adsorption capacity towards Pb(II).

Based on the above XPS spectra and DFT calculations, the adsorption of Pb(II) on e-TACFs and e-TACSs can be explained by the following reactions. At pH < 7, $Pb^{2+}$ was the only aqueous species (Fig. 6d), so the ion-exchange reaction and the surface complexation reaction can be described as eqn (9) and (10), respectively. Under strong acid conditions, the competitive reaction of $H^+$ was also considered and is described as eqn (11).

$$2[\equiv Ti\text{–}O]^-Na^+ + Pb^{2+} \rightleftharpoons Pb^{2+}([\equiv Ti\text{–}O]^-)_2 + 2Na^+ \quad (9)$$

$$2\equiv Ti\text{–}OH + Pb^{2+} \rightleftharpoons (\equiv Ti\text{–}O)_2Pb + 2H^+ \quad (10)$$

$$[\equiv Ti\text{–}O]^-Na^+ + H^+ \rightleftharpoons [\equiv Ti\text{–}O]^-H^+ + Na^+ \quad (11)$$

At 7 < pH < 9.5, different species of lead-hydroxylated complexes were formed, thus the ion-exchange reactions took place in the form of eqn (12) and (13), while the surface complexation reactions can be described as eqn (14) and (15).

$$[\equiv Ti\text{–}O]^-Na^+ + Pb(OH)^+ \rightleftharpoons Na^+ + [\equiv Ti\text{–}O]^-Pb(OH)^+ \quad (12)$$

$$2[\equiv Ti\text{–}O]^-Na^+ + Pb_3(OH)_4{}^{2+} \rightleftharpoons ([\equiv Ti\text{–}O]^-)_2Pb_3(OH)_4{}^{2+} + 2Na^+ \quad (13)$$

$$\equiv Ti\text{–}OH + Pb(OH)^+ \rightleftharpoons H^+ + \equiv Ti\text{–}OPb(OH) \quad (14)$$

$$2\equiv Ti\text{–}OH + Pb_3(OH)_4{}^{2+} \rightleftharpoons (\equiv Ti\text{–}O)_2Pb_3(OH)_4 + 2H^+ \quad (15)$$

At pH > 9.5, $Pb(OH)_3^-$ became the dominant species; eqn (16) might be the possible reaction mechanism.

$$\equiv Ti\text{–}OH + Pb(OH)_3{}^- + OH^- \rightleftharpoons H_2O + (\equiv Ti\text{–}O)Pb(OH)_3{}^{2-} \quad (16)$$

## Conclusions

In summary, etched $Ti_3AlC_2$ nanofibers and nanosheets were synthesized by a fluoride-free and simple one-step hydrothermal method. The characterization results demonstrated that the etched $Ti_3AlC_2$ samples obtained by varying the NaOH concentration presented different morphologies (nanofibers and nanosheets) and specific surface areas. The as-synthesized materials exhibited a high adsorption capacity for Pb(II) in solution. The adsorption processes were strongly dependent on pH and ionic strength and the thermodynamic studies showed spontaneous and endothermic adsorption processes. In particular, the XPS analysis revealed the underlying interaction mechanism with Pb(II), which was mainly dominated by outer-sphere surface complexation and cation exchange. Compared with the e-TACSs, the e-TACFs showed a higher adsorption capacity for Pb(II), which was attributed to the remarkably enhanced specific surface area and stronger surface complexation affinity with Pb(II). The DFT calculations further manifested that the etched $Ti_3AlC_2$ had a strong adsorption capacity towards Pb(II). The findings herein not only highlight the fluoride-free production of well-structured etched $Ti_3AlC_2$ but also open a new perspective for the preparation of other functional 2D-MXene materials for environmental pollution clean-up.

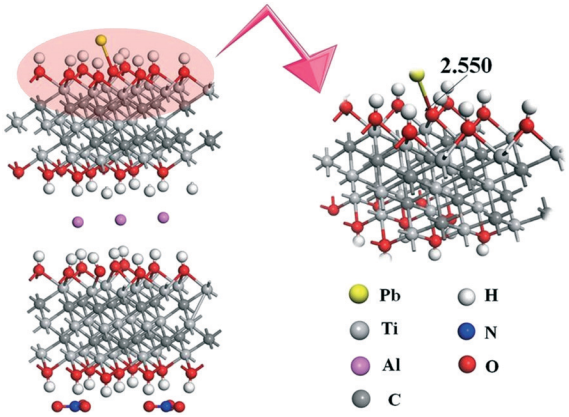


Fig. 9 The optimized structures for Pb(II) adsorbed on etched $Ti_3AlC_2$; the representative bond length is in Å.

## Conflicts of interest

There are no conflicts to declare.

## Acknowledgements

The financial support from the National Key Research and Development Program of China (2017YFA0207002), the NSFC (21607042, 21577032, and 21777039), the National Special Water Programs (2015ZX07203-011 and 2015ZX07204-007), the Fundamental Research Funds for the Central Universities (2018ZD11, 2018MS114, 2017YQ001, 2017XS094, and 2017MS045), the Jiangsu Provincial Key Laboratory of Radiation Medicine and Protection and the Priority Academic Program Development of Jiangsu Higher Education Institutions is acknowledged. X. Wang acknowledges the CAS Interdisciplinary Innovation Team of the Chinese Academy of Sciences.

## References

1 X. L. Yu, D. J. Kang, Y. Y. Hu, S. R. Tong, M. F. Ge, C. Y. Cao and W. G. Song, *RSC Adv.*, 2014, **4**, 31362–31369.

 

2 X. L. Yu, S. R. Tong, M. F. Ge, L. Wu, J. C. Zuo, C. Y. Cao and W. G. Song, *J. Environ. Sci.*, 2013, **25**, 933–943.
3 Y. M. Liu, X. J. Ju, Y. Xin, W. C. Zheng, W. Wang, J. Wei, R. Xie, Z. Liu and L. Y. Chu, *ACS Appl. Mater. Interfaces*, 2014, **6**, 9530–9542.
4 C. H. Yan, J. Xu and X. M. Shen, *Environ. Health Perspect.*, 2013, **121**, A294–296.
5 H. N. Kim, W. X. Ren, J. S. Kim and J. Y. Yoon, *Chem. Soc. Rev.*, 2012, **41**, 3210–3244.
6 D. J. Kang, X. L. Yu, M. F. Ge and W. G. Song, *Microporous Mesoporous Mater.*, 2015, **207**, 170–178.
7 M. H. Liu, Y. H. Wang, L. T. Chen, Y. Zhang and Z. Lin, *ACS Appl. Mater. Interfaces*, 2015, **7**, 7961–7969.
8 T. Wen, X. L. Wu, X. L. Tan, X. K. Wang and A. W. Xu, *ACS Appl. Mater. Interfaces*, 2013, **5**, 3304–3311.
9 Q. R. Zhang, J. Teng, G. D. Zou, Q. M. Peng, Q. Du, T. F. Jiao and J. Y. Xiang, *Nanscale.*, 2016, **8**, 7085–7093.
10 G. D. Zou, J. X. Guo, Q. M. Peng, A. G. Zhou, Q. R. Zhang and B. Z. Liu, *J. Mater. Chem. A*, 2016, **4**, 489–499.
11 N. Abdullah, R. Gohari, N. Yusof, A. Ismail, J. Juhana, W. J. Lau and T. Matsuura, *Chem. Eng. J.*, 2016, **289**, 28–37.
12 J. Hu, X. L. Tan, X. M. Ren and X. K. Wang, *Dalton Trans.*, 2012, **41**, 10803–10810.
13 L. Chu, C. B. Liu, G. Y. Zhou, R. Xu, Y. H. Tang, Z. B. Zeng and S. L. Luo, *J. Hazard. Mater.*, 2015, **300**, 153–160.
14 G. X. Zhao, J. Li, X. M. Ren, C. L. Chen and X. K. Wang, *Environ. Sci. Technol.*, 2011, **45**, 10454–10462.
15 Y. B. Sun, D. D. Shao, C. L. Chen, S. T. Yang and X. K. Wang, *Environ. Sci. Technol.*, 2013, **47**, 9904–9910.
16 O. Mashtalir, M. Naguib, V. N. Mochalin, Y. Dall'Agnese, M. Heon, M. W. Barsoum and Y. Gogotsi, *Nat. Commun.*, 2013, **4**, 1716–1722.
17 M. Naguib and Y. Gogotsi, *Acc. Chem. Res.*, 2014, **48**, 128–135.
18 M. Naguib, J. Come, B. Dyatkin, V. Presser, P. L. Taberna, P. Simon, M. W. Barsoum and Y. Gogotsi, *Electrochem. Commun.*, 2012, **16**, 61–64.
19 M. R. Lukatskaya, O. Mashtalir, C. E. Ren, Y. Dall'Agnese, P. Rozier, P. L. Taberna, M. Naguib, P. Simon, M. W. Barsoum and Y. Gogotsi, *Science*, 2013, **341**, 1502–1505.
20 T. Y. Ma, J. L. Cao, M. Jaroniec and S. Z. Qiao, *Angew. Chem., Int. Ed.*, 2016, **55**, 1138–1142.
21 Y. L. Ying, Y. Liu, X. Y. Wang, Y. Y. Mao, W. Cao, P. Hu and X. S. Peng, *ACS Appl. Mater. Interfaces*, 2015, **7**, 1795–1803.
22 A. K. Fard, G. McKay, R. Chamoun, T. Rhadfi, H. Preud'Homme and M. A. Atieh, *Chem. Eng. J.*, 2017, **317**, 331–342.
23 M. Naguib, M. Kurtoglu, V. Presser, J. Lu, J. Niu, M. Heon, L. Hultman, Y. Gogotsi and M. W. Barsoum, *Adv. Mater.*, 2011, **23**, 4248–4253.
24 P. E. Blöchl, *Phys. Rev. B: Condens. Matter Mater. Phys.*, 1994, **50**, 17953–17979.
25 G. Kresse and D. Joubert, *Phys. Rev. B: Condens. Matter Mater. Phys.*, 1999, **59**, 1758–1775.
26 D. Chadi, *Phys. Rev. B: Solid State*, 1977, **16**, 1746–1947.
27 J. E. Spanier, S. Gupta, M. Amer and M. W. Barsoum, *Phys. Rev. B: Condens. Matter Mater. Phys.*, 2005, **71**, 012103–012106.
28 X. H. Xie, Y. Xue, L. Li, S. G. Chen, Y. Nie, W. Ding and Z. D. Wei, *Nanoscale*, 2014, **6**, 11035–11040.
29 Q. M. Peng, J. X. Guo, Q. R. Zhang, J. Y. Xiang, B. Z. Liu, A. G. Zhou, R. P. Liu and Y. J. Tian, *J. Am. Chem. Soc.*, 2014, **136**, 4113–4116.
30 M. K. Han, X. W. Yin, H. Wu, Z. X. Hou, C. Q. Song, X. L. Li, L. T. Zhang and L. F. Cheng, *ACS Appl. Mater. Interfaces*, 2016, **8**, 21011–21019.
31 X. F. Wang, X. Shen, Y. R. Gao, Z. X. Wang, R. C. Yu and L. Q. Chen, *J. Am. Chem. Soc.*, 2015, **137**, 2715–2721.
32 L. Yin, P. Y. Wang, T. Wen, S. J. Yu, X. X. Wang, T. Hayat, A. Alsaedi and X. K. Wang, *Environ. Pollut.*, 2017, **226**, 125–134.
33 S. T. Yang, G. D. Sheng, Z. Q. Guo, X. L. Tan, J. Z. Xu and X. K. Wang, *Sci. China: Chem.*, 2012, **55**, 632–642.
34 H. Chen, X. X. Wang, J. Li and X. K. Wang, *J. Mater. Chem. A*, 2015, **3**, 6073–6081.
35 J. Wang, D. J. Kang, X. L. Yu, M. F. Ge and Y. T. Chen, *Chem. Eng. J.*, 2015, **264**, 506–513.
36 W. Yao, S. J. Yu, J. Wang, Y. D. Zou, S. S. Lu, Y. J. Ai, N. S. Alharbi, A. Alsaedi, T. Hayat and X. K. Wang, *Chem. Eng. J.*, 2017, **307**, 476–486.
37 J. Wang, X. X. Wang, L. Q. Tan, Y. T. Chen, T. Hayat, J. Hu, A. Alsaedi, B. Ahmad, W. Guo and X. K. Wang, *Chem. Eng. J.*, 2016, **297**, 106–115.
38 C. Y. Jing, J. L. Cui, Y. Y. Huang and A. G. Li, *ACS Appl. Mater. Interfaces*, 2012, **4**, 714–720.
39 G. X. Zhao, X. M. Ren, X. Gao, X. Tan, J. X. Li, C. L. Chen, Y. Y. Huang and X. K. Wang, *Dalton. Trans.*, 2011, **40**, 10945–10952.
40 Y. B. Sun, S. T. Yang, G. D. Sheng, Z. Q. Guo and X. K. Wang, *J. Environ. Radioact.*, 2012, **105**, 40–47.
41 Z. Reddad, C. Gerente, Y. Andres and P. Cloirec, *Environ. Sci. Technol.*, 2002, **36**, 2067–2073.
42 C. L. Chen, X. X. Wang and X. K. Wang, *Ind. Eng. Chem. Res.*, 2006, **45**, 9144–9149.
43 K. L. Mercer and J. E. Tobiason, *Environ. Sci. Technol.*, 2008, **42**, 3797–3802.
44 X. S. Wang, J. Huang, H. Q. Hu, J. Wang and Y. Qin, *J. Hazard. Mater.*, 2007, **142**, 468–476.
45 S. Chen, W. M. Liu and L. G. Yu, *Wear*, 1998, **218**, 153–158.
46 A. Volpe, M. Pagano, C. Pastore, C. Cuocci and A. Milella, *J. Environ. Sci. Health, Part A: Toxic/Hazard. Subst. Environ. Eng.*, 2016, **51**, 1121–1130.